



A STUDY ON THE APPLICATION OF THE MASS-CONSISTENT WIND FIELD MODEL THROUGH HIGH-RESOLUTION WIND FIELD SIMULATION AROUND THE INCHEON INTERNATIONAL AIRPORT OF KOREA

Young-Gon Lee¹, Jia Jung², Geun-Hoi Kim³, Baek-Jo Kim⁴

Abstract- The mass-consistent wind field model (MCWFM) is applied to simulate high resolution of 100 m wind fields around the Incheon International Airport (IIA), Korea. In this study, three types of input data, that are the 5-m resolution Digital Elevation Model (DEM) data, model output of Korea Meteorological Administration (KMA)'s operational Local Data Assimilation and Prediction System (LDAPS), and seventeen weather observations around airport, are used to produce three dimensional wind flow for a wind gust event issued at the airport during 3 – 5 of May, 2016.

This model validation is also performed by estimating the wind data at each of the virtually subtracted observation points that make up the Low Level Wind-shear Alter System (LLWAS) in IIA, and then by the results to the their original measurements in turn. Especially, the mean value of the wind speed is 7.9 m/s, which was very similar for the average of 8.4 m/s from the same wind speed measurements, and the R-squared value of the wind speed shows MCWFM presents better estimation of 96.2 % to the observations than LDAPS of 66.9 %.

The results show that wind fields computed from the MCWFM are more realistic near the hilly area, and well matched to the measurements at the airport during the extreme weather event. Furthermore, given the production of 100-m resolution three-dimensional wind field data within eight minutes and its further use of input data for high-resolution forecasting models, the MCWFM could be very useful for simulating wind flow in the runway in support of wind hazardous management in airports.

Keywords – Mass-Consistent Wind Field Model (MCWFM), wind simulation, wind gust

1. INTRODUCTION

Sudden changes of air flow or turbulence are a well-known hazard to both aircraft operation and airport management. In particular, wind gust and shear in low-level atmosphere could be responsible for numerous accidents during the takeoff or landing phase of flight at the airport (Wong et al., 2013; Chan and Hon, 2016). The Federal Aviation Administration (2010) reported 47 that weather events either caused or contributed to 2,223 (20.1%) out of 8,657 aviation 48 accidents during 2003–2009. Statistics showed that wind was the leading factor in weather-49 related aviation accidents, accounting for 53.4% (1,047) of these accidents.

It is generally needed to provide accurate wind information to aviation users such as pilots, dispatchers, and air traffic controllers to assure safety of flights and reduce schedule delay and air traffic management problems. Hence, a fine-scale wind simulation system is also essential to provide improved guidance on the turbulent flow within such limited area of airport (Regmi et al., 2014; Reiche et al., 2015). Because such high-resolution wind simulation practically requires significant computing resources and complexity of data process, several methods and strategies, with various level of complexity, have been proposed to address the problems (Juárez et al., 2012). There are two general model types: prognostic models and diagnostic models. While the prognostic models is used to calculate realistic and future atmospheric state over computing capacity and time, the diagnostic models can be useful for short-term wind flow state estimation with simple model equations in a very short time (Ratto, 1996).

Among many types of diagnostic models, the mass-consistent wind field model (MCWFM) has been readily applied to many practical situations, such as the siting of wind turbines, or as input in the estimation of diffusion and transport of pollutants over the complex terrain (Castino et al., 2003; Wang et al., 2005). Despite its simple model dynamics, it can represent more accurate three-dimensional atmospheric flow, and recently is used to make microscale (about 1 m) initial wind field by coupling with a local prognostic model (Oliver et al., 2012). Thus, this diagnostic model can be very useful for quickly analyzing or presenting the timing and severity of wind hazards at airports because it is simple and accurate and can be used in high resolution wind predictions.

In this study, we applied the MCWFM to simulate 100-m resolution 3-D wind fields around the Incheon International Airport (IIA), Korea. The results were compared not only to the weather measurements but also to 3-D analysis wind data from the

^{1,2,3,4} Applied Meteorology Research Division, National Institute of Meteorological Sciences, Seogwipo, Jeju-do, Republic of Korea

operational local-scale forecast system of Korea Meteorological Administration (KMA). For technical details, section 2 first discusses the methodology of how input data are processed, and then describes the model formulation to calculate the wind simulation of 100 m resolution. Section 3 presents the results of diagnostic wind fields and verification for an event case of wind gust at the airport on May 2016. Finally, summary and concluding remarks are drawn in Session 4.

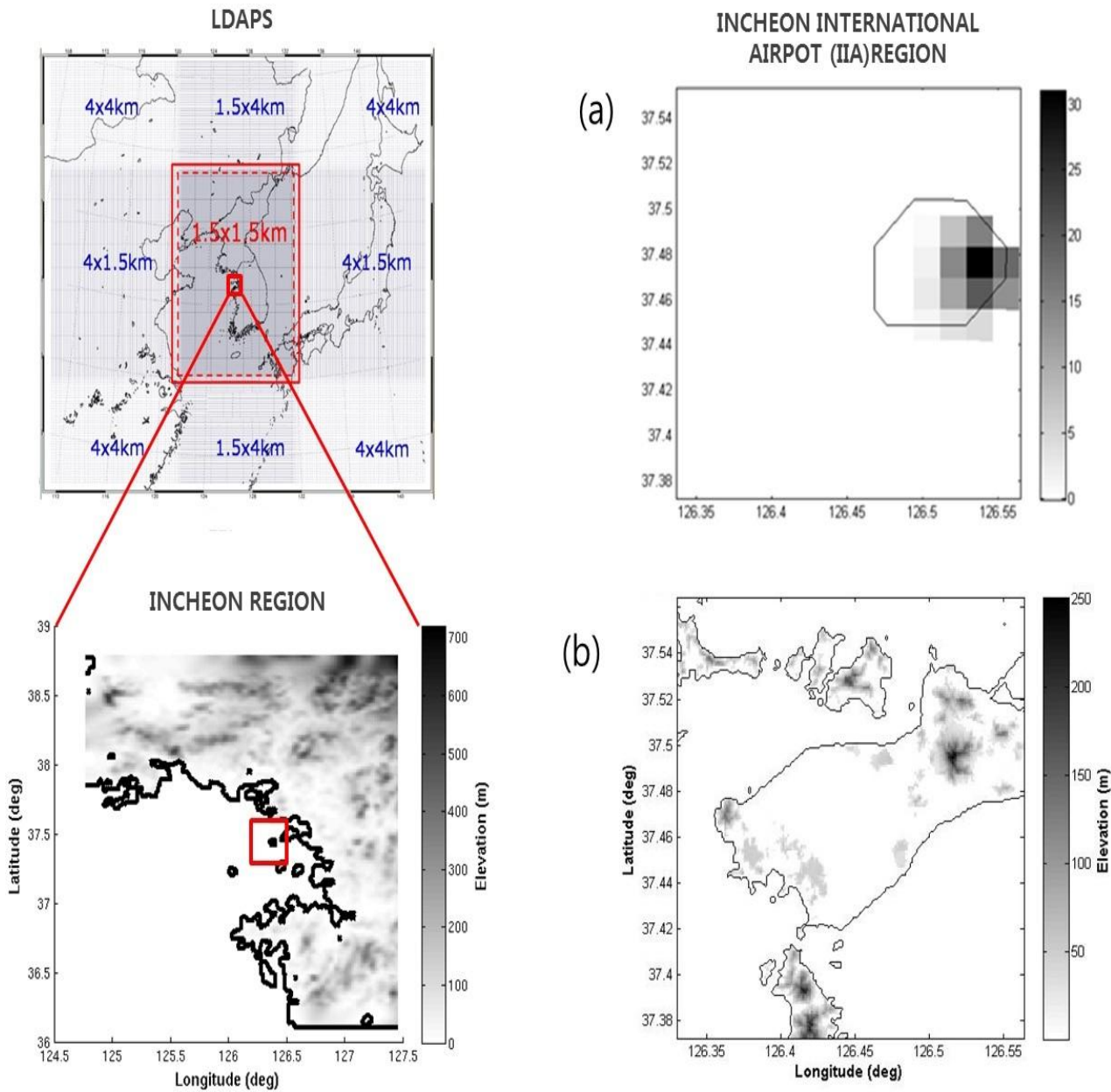
2. METHODS

Generally, the MCWFM is based on the principle of mass conservation in which divergence is eliminated from an initial wind field. Given a number of wind measurements and any coarser model data, the MCWFM physically interpolates in such a way that the estimation process satisfies this mass conservation, and then produces very detailed wind field over a certain area.

2.1 Input data –

Three types of data set are used to generate fine-scale wind data around the IIA region. The first is LDAPS output, which are three-dimensional and surface data covers the Korean peninsula with 744×928 grid points (left plate of Fig.1). This local prediction system produces 36-hour (0000, 0600, 1200, 1800 UTC) and 3-hour forecasts (0300, 0900, 1500, 2100 UTC) in every four times a day respectively. The LDAPS output consists of 70-level (from 2 m to 37.9 km) analysis (h00 forecast) and 36-/3-hour forecast (h01-h36/h01-h03 forecasts) data for each model running time. Analysis fields classified as ‘h00’ in each model output are used to the MCWFM for simulating the 15-level (from 2 m to 500 m) wind field of around the airport. As a second input material, wind observations from five Automated Weather Station (AWS) systems and twelve anemometers (wind sensors) consisting of the Low Level Wind Alert System (LLWAS) are also allowed for the MCWFM winds simulation. All measurements are provided through the KMA’s real-time data quality management system (Heo et al., 2005).

The orography data entered to the LDAPS can’t consider the real surface characteristics around the airport opened at March 2001, because it consists of 1-km resolution surface information made from International Geosphere Biosphere Program (IGBP) conducted from 1993 to 2000. It is illustrated in Figure 1(a) that these incorrect terrain data are entered into the LDAPS. Finally, in order to produce more accurate surface and altitude information, the 5-m resolution Digital Elevation Model (DEM) data released from the National Geographic Information Institute (NGII) of Korea on 2013 was used to generate a new topography covering IIA (Fig.1(b)). The grid is designated by Transverse Mercator (TM) coordinates (Table 1) in the $21 \text{ km} \times 21 \text{ km}$ domain area of $126.330^\circ \text{ E} \sim 126.564^\circ \text{ E}$ in east-west and $37.372^\circ \text{ N} \sim 37.564^\circ \text{ N}$ in the north-south directions. Figure 2 shows that small islands such as Yongyudo, Jangbongdo, Muuido, and Sindo distributed around IIA, and airport region including the runways are omitted in the LDAPS orography. In contrast to the LDAPS, the newly generated topography gives much more substantial and provides improved land surface information.



(Left) Schematic diagram of model domain nested down from LDAPS to Incheon region located at the western coast of the Korean peninsula. (Right) Expanded orography data of (a) LDAPS and (b) MCWFM indicated as red rectangular in the lower-left hand figure. Both of model domains cover the same area of 21 km X 21 km (latitude : 37.37° N - 37.56° N, longitude : 126.33° E - 126.56° E) around IIA region. The gray color bar indicates topographical height over the model domains.

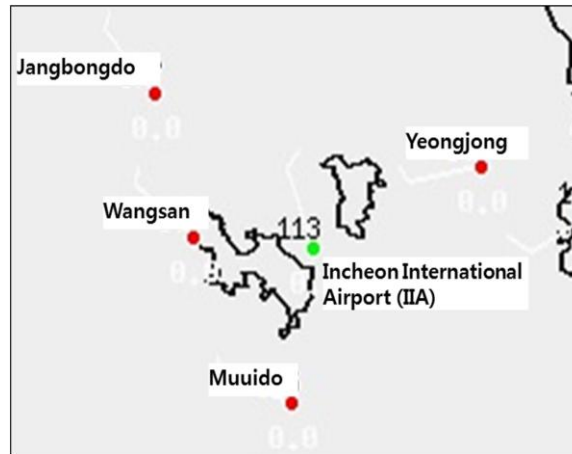
2.2. Watermark Extraction algorithm –

A three-dimensional mass-consistent wind field model is used to produce high resolution winds around IIA. The wind measurements and the LDAPS output are used to construct initial gridded winds of a 100-m resolution in the model domain. Initial guesses of three-dimensional wind components, (u0, v0, w0) in (i, j, k) coordinate system over the fine domain are formed from the weighted interpolation scheme (hence the Cressman interpolation) for the existing observed and simulated wind data (up, vp, wp) at p-th input data points (Goodin et al., 1979),

Table -1 Description of the three orography data (DEM, LDAPS, and this study)

DEM		LDAPS		This study	
Projected	Coordinate	Transverse Mercator	Lambert	Conformal	Transverse Mercator

System	Conic		
Resolution	5 m	1.5 km	10 m (2,101 x 2,010), 100m (210 x 210)
Areal range	37.372° ~ 37.564°, 126.330° ~ 126.564° (21km x 21km)		



The five AWS stations (red dots - Wangsan, Yeongjong, Jangbongdo, and Muuido; green dot - IIA) considered in wind field simulation around the airport.

$$(U_0, V_0, W_0) = \frac{\sum_{p=1}^{np} \omega(U_0 - U_p, V_0 - V_p, W_0 - W_p) (U_p, V_p, W_p)}{\sum_{p=1}^{np} \omega(U_0 - U_p, V_0 - V_p, W_0 - W_p)} \quad (1)$$

and the weight function (ω) is obtained from the inversed square of the difference between two wind values,

$$\omega(U_0 - U_p, V_0 - V_p, W_0 - W_p) = \frac{1}{d(U_0 - U_p, V_0 - V_p, W_0 - W_p)^2} \quad (2)$$

The model then is to minimize the difference between the initial wind components (u_0, v_0, w_0) and adjusted wind components (u, v, w) so that the equation,

$$E(u, v, w) = \iiint [\alpha_1^2 (u - u_0)^2 + \alpha_1^2 (v - v_0)^2 + \alpha_2^2 (w - w_0)^2] dV \quad (3)$$

satisfies the constraint that the divergence should vanish, and the continuity equation,

$$\frac{\partial u}{\partial x} + \frac{\partial v}{\partial y} + \frac{\partial w}{\partial z} = 0 \quad (4)$$

In equation (3), α_1 and α_2 are Gauss moduli that are used to determine the relative adjustment to be made between the horizontal and vertical wind components respectively.

Using Lagrange multiplier theory, the constraint equation (3) becomes one of minimizing the modified functional,

$$F(u, v, w, \lambda) =$$

$$\iiint \left[\alpha_1^2 (u - u_0)^2 + \alpha_1^2 (v - v_0)^2 + \alpha_2^2 (w - w_0)^2 + \lambda \left(\frac{\partial u}{\partial x} + \frac{\partial v}{\partial y} + \frac{\partial w}{\partial z} \right) \right] dV, \tag{5}$$

where $\lambda(x,y,z)$ is a Lagrange multiplier. The associated Euler-Lagrange equations whose solution minimize (5) are

$$u = u_0 + \frac{1}{2\alpha_1^2} \frac{\partial \lambda}{\partial x}, \quad v = v_0 + \frac{1}{2\alpha_1^2} \frac{\partial \lambda}{\partial y}, \quad w = w_0 + \frac{1}{2\alpha_2^2} \frac{\partial \lambda}{\partial z}, \tag{6}$$

which are subject to $n_x \lambda (u-u_0) = \lambda n_x \delta u = 0$, $n_y \lambda (v-v_0) = \lambda n_y \delta v = 0$, and $n_z \lambda (w-w_0) = \lambda n_z \delta w = 0$ on the x , y , and z boundary respectively. This condition suggests either $\lambda=0$ (a “free flow” condition) or the normal components of flow at the boundary remain unchanged following the adjustment where n_x , n_y , and n_z are defined as the outward positive unit normal of the directions x , y , and z (Sherman, 1978). Assuming that α_1 and α_2 are constant in whole of the domain, substitution of (6) into (5) yields the governing equation for λ :

$$\frac{\partial^2 \lambda}{\partial x^2} + \frac{\partial^2 \lambda}{\partial y^2} + \left(\frac{\alpha_1}{\alpha_2} \right) \frac{\partial^2 \lambda}{\partial z^2} = -2\alpha_1^2 \left(\frac{\partial u_0}{\partial x} + \frac{\partial v_0}{\partial y} + \frac{\partial w_0}{\partial z} \right). \tag{7}$$

This equation is solved for λ with the above boundary conditions and the adjusted velocity field is calculated using (6).

Finally, the wind components (u , v , w) are computed in the terrain-following coordinate system where a new vertical coordinate σ is related to z through the relationship,

$$x^* = x, \quad y^* = y, \quad \sigma = \frac{z_t - z}{z_t - z_s} = \frac{z_t - z}{\pi}, \tag{8}$$

where z_t is the top of the model, assumed to be a constant altitude and z_s is the height of the terrain surface, which is a function of x and y (Traci et al., 1978). The use of this coordinate allows better representation of the surface topography and more accurate treatment of the bottom boundary (Kitada et al., 1983). Therefore, as shown by Barnard et al. (1987), the continuity equation (4) in the transformed coordinate is

$$\frac{\partial \pi u}{\partial x} + \frac{\partial \pi v}{\partial y} + \frac{\partial \pi w^*}{\partial \sigma} = 0, \tag{9}$$

where

$$\pi w^* = \sigma \left(\frac{\partial z_s}{\partial x} u + \frac{\partial z_s}{\partial y} v \right) - w. \tag{10}$$

Rearranging the governing equation (7), the Poisson equation for λ can be obtained as follows

$$\begin{aligned} & \frac{\partial}{\partial x} \left(\pi \frac{\partial \lambda}{\partial x} + \sigma \frac{\partial z_s}{\partial x} \frac{\partial \lambda}{\partial \sigma} \right) + \frac{\partial}{\partial y} \left(\pi \frac{\partial \lambda}{\partial y} + \sigma \frac{\partial z_s}{\partial y} \frac{\partial \lambda}{\partial \sigma} \right) \\ & + \frac{\partial}{\partial \sigma} \left\{ \left[\frac{\alpha_1^2}{\alpha_2^2} + \sigma^2 \left[\left(\frac{\partial z_s}{\partial x} \right)^2 + \left(\frac{\partial z_s}{\partial y} \right)^2 \right] \right\} \times \frac{1}{\pi} \frac{\partial \lambda}{\partial \sigma} + \sigma \left(\frac{\partial z_s}{\partial x} \frac{\partial \lambda}{\partial x} + \frac{\partial z_s}{\partial y} \frac{\partial \lambda}{\partial y} \right) \right\} \\ & = -2\alpha_1^2 \left(\frac{\partial \pi u_0}{\partial x} + \frac{\partial \pi v_0}{\partial y} + \frac{\partial \pi w_0^*}{\partial z} \right), \end{aligned} \tag{11}$$

and the adjusted velocity components (u , v , w) is solved by

$$u = u_0 + \frac{1}{2\alpha_1^2} \left(\frac{\partial \lambda}{\partial x} + \frac{\sigma}{\pi} \frac{\partial z_s}{\partial x} \frac{\partial \lambda}{\partial \sigma} \right), \tag{12}$$

$$v = v_0 + \frac{1}{2\alpha_1^2} \left(\frac{\partial \lambda}{\partial y} + \frac{\sigma}{\pi} \frac{\partial z_s}{\partial y} \frac{\partial \lambda}{\partial \sigma} \right), \tag{13}$$

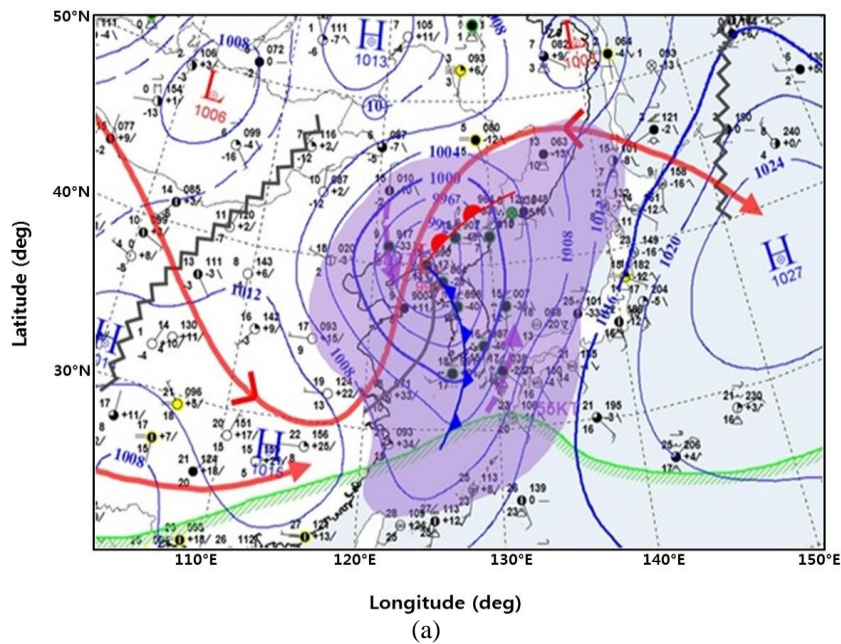
$$w = w_0 - \frac{1}{2\alpha_2^2} \left(\frac{1}{\pi} \frac{\partial \lambda}{\partial \sigma} \right) \tag{14}$$

The final wind velocities over the 100-m resolution grid domain are obtained numerically by equation (12) – (14) using the calculated λ (Ishikawa, 1994).

3. RESULTS

For the MCWFM verification, the wind fields obtained from the model are compared to the five AWS observations (e.g., Incheon airport, Wangsan, Yeongjong, Jangbongdo, and Muuido) around IIA region for a strong wind event occurred from 1700 UTC May 2 to 1000 UTC May 4, 2016. The 100-m wind field simulation is conducted using LDAPS analysis data (00 hour forecasts) at each 3-hour time interval, and it takes within 8 minutes after LDAPS was carried out. The MCWFM wind output is calculated directly from the LDAPS analysis output of 10-m height, which is the same altitude of the AWS measurements around the airport. In contrast, the wind data that corresponds to the LLWAS observation altitude is interpolated and calculated by using the cubic spline interpolation method for the wind data between 13 m and 33 m altitude in three-dimensional LDAPS data (Fritsch, 1971). Both of simulation and observation used in comparison are instantaneous for each correspondence time.

Figure 3 shows synoptic charts around the Korean peninsula during the high wind case. A cyclone passed through the region, and westerly winds became stronger as the low-pressure system developed and isobaric lines narrowed for a 12-h time period on May 3, 2016. During the impact of the west wind, the air temperatures measured at the five AWSs decreased to 10°C as cold air was blown over IIA region, but increased to 15°C when relatively warm air was blown from the south after the low-pressure system had passed at 0900 UTC on May 4, 2016 (Fig. 4(a)). The wind speed of Wangsan AWS showed a maximum wind speed of 19.6 m/s (thick blue line of Fig. 4(b)), which was close to the high-wind warning level of 21.0 m/s, around 1200 UTC on May 3, 2006. A high-wind watch was issued during the high-wind event at the airport, as the observed wind speed exceeded 14.0 m/s as measured by the IIA AWS (the black line of Fig 4(b)) from 1200 UTC to 1800 UTC on May 3, 2016. Wind direction shown in Fig.4(c) changed from a southerly to a westerly direction with the passage of the cyclone, and westerly winds dominated over the airport during the event.



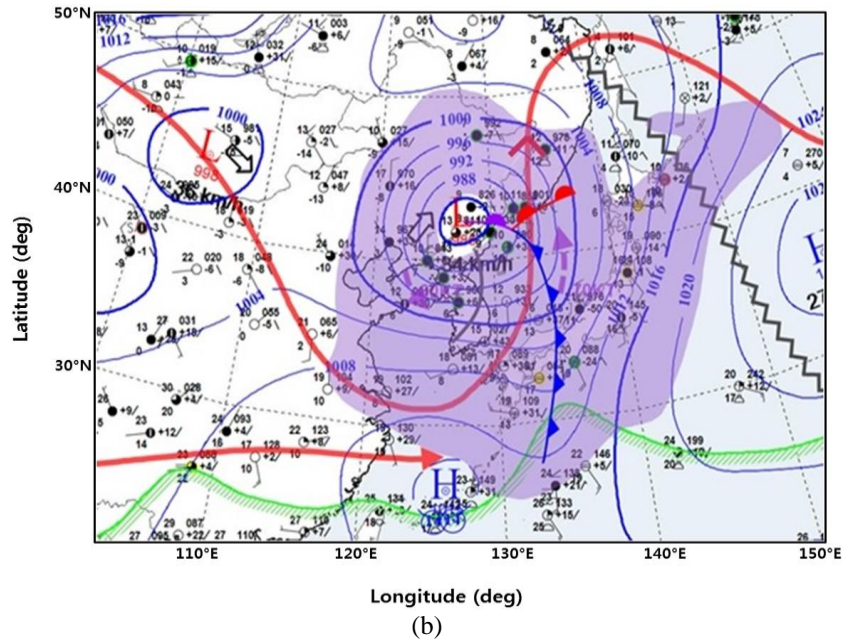
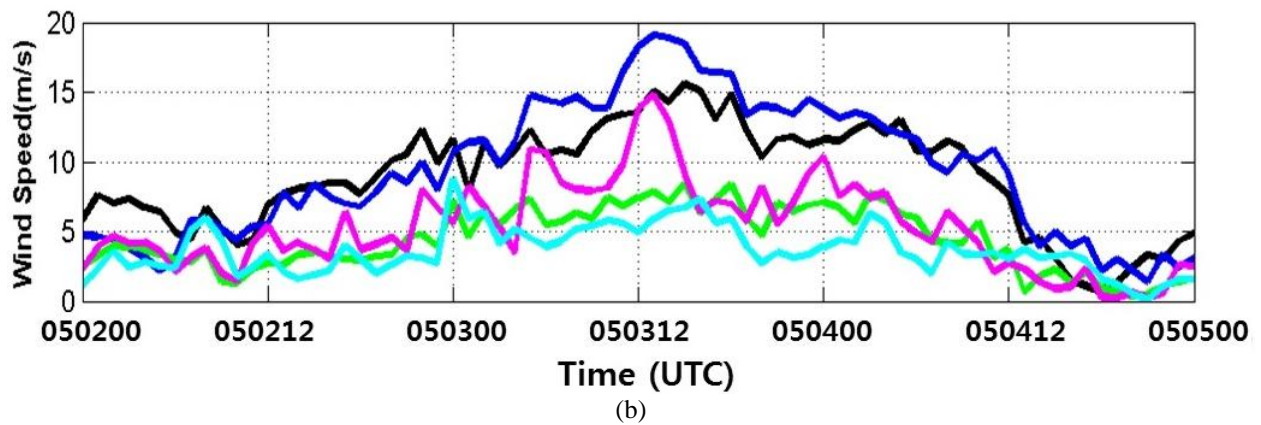
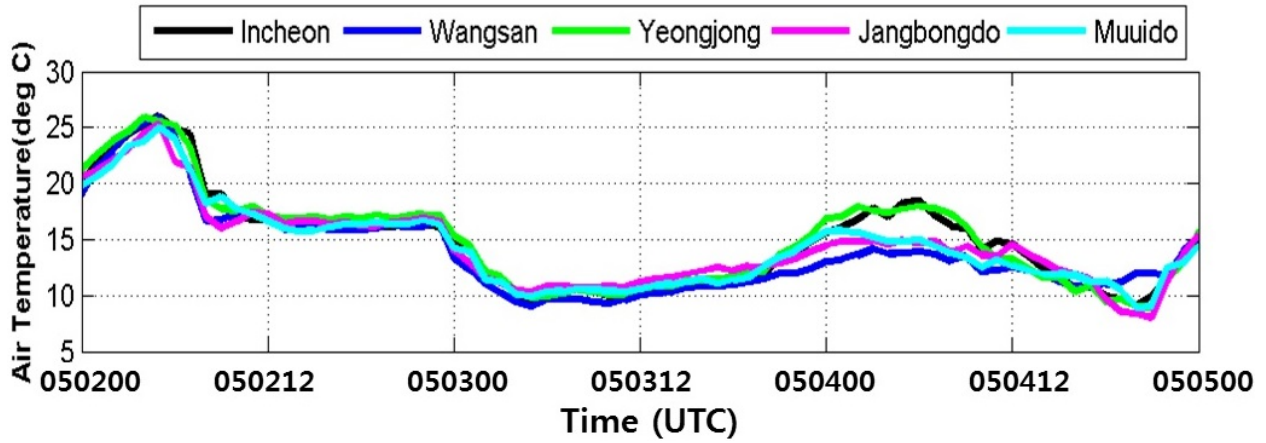


Figure 3. Synoptic weather charts over the Korean peninsula on (a) 0000 UTC and (b) 1200 UTC 3 May 2016, when the strong wind speed event was observed at the Incheon International Airport, Korea. The solid blue contours, thick red curves, and a shaded green light line present isobaric, jet stream, and dew point temperature of 20 °C respectively.



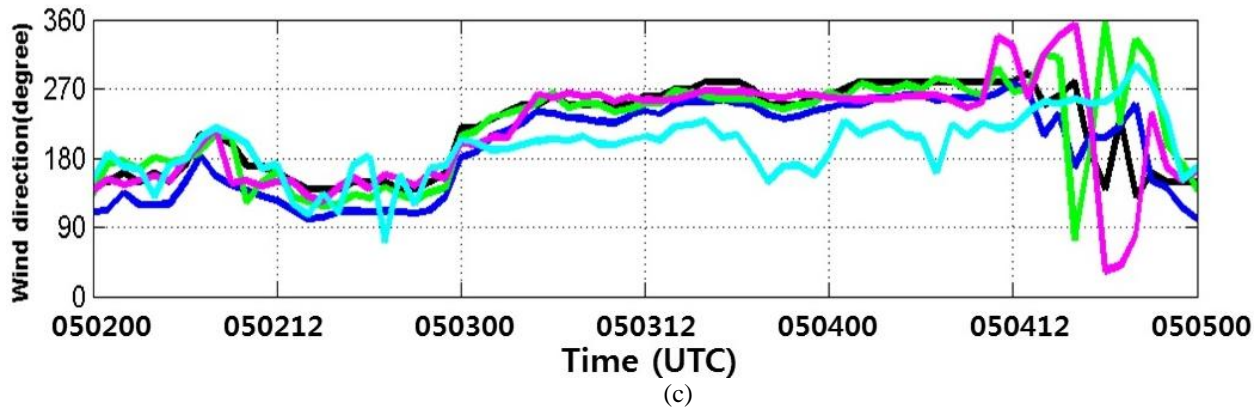
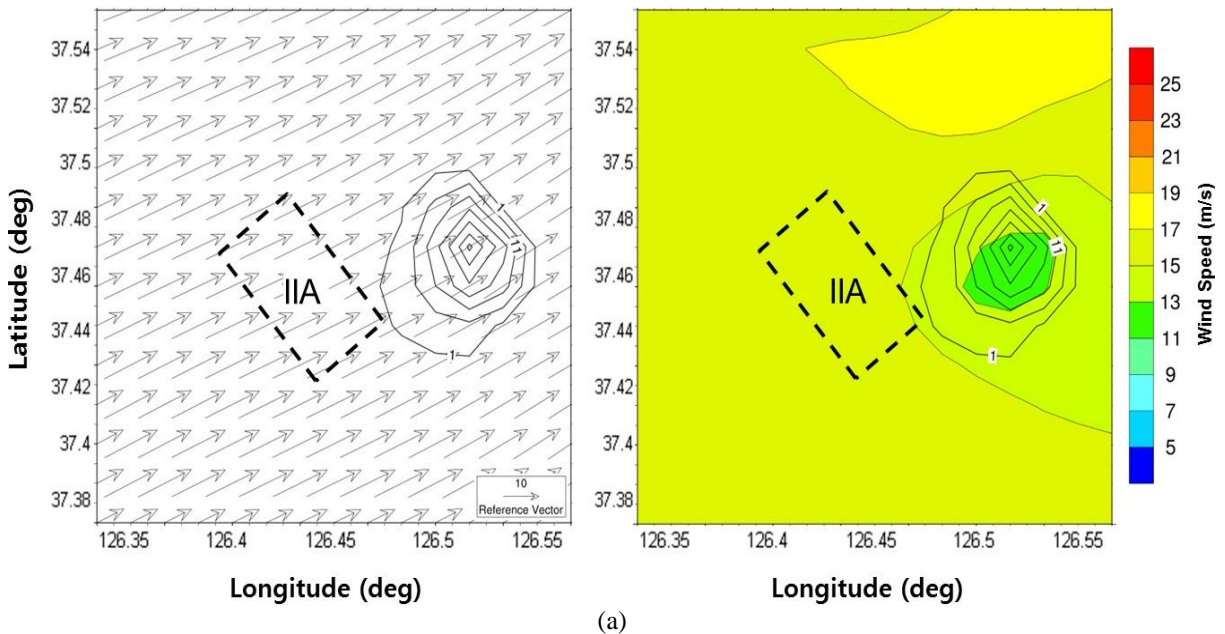


Figure 4. Temporal variations of (a) temperature, (b) wind speed, and (c) wind direction at the five AWS stations around the Incheon International Airport during the strong wind event (from 0000UTC May 2 to 0000 UTC May 5, 2016)

Wind fields from the LDAPS 1.5 km analysis output are presented at 10-m height for the strong wind event on 1200 UTC May 3 and 0000 UTC May 4 2016 (Fig. 5a). The figure illustrates that southwesterly winds larger than 15.0 m/s are dominated over most domain region, and this main flow is kept in the model domain after 6 hours. It is also shown that somewhat decrease of wind speed at the east part of the small hill on 1200 UTC May 3. The region of wind decrease is shifted to the north part as the cyclone system moving at twelve hours later (0000 UTC May 4). Nevertheless, the wind direction and speed in the airport area (a dashed rectangular in Fig. 5) do not changed in the LDAPS simulation during the 12-hours.



(a)

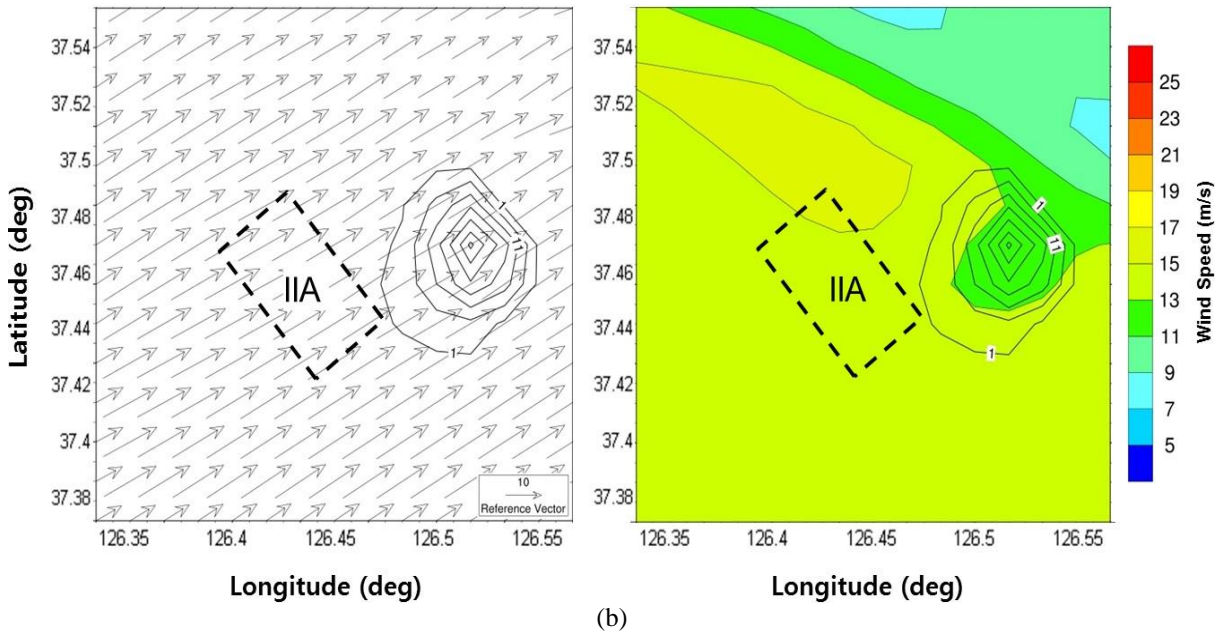
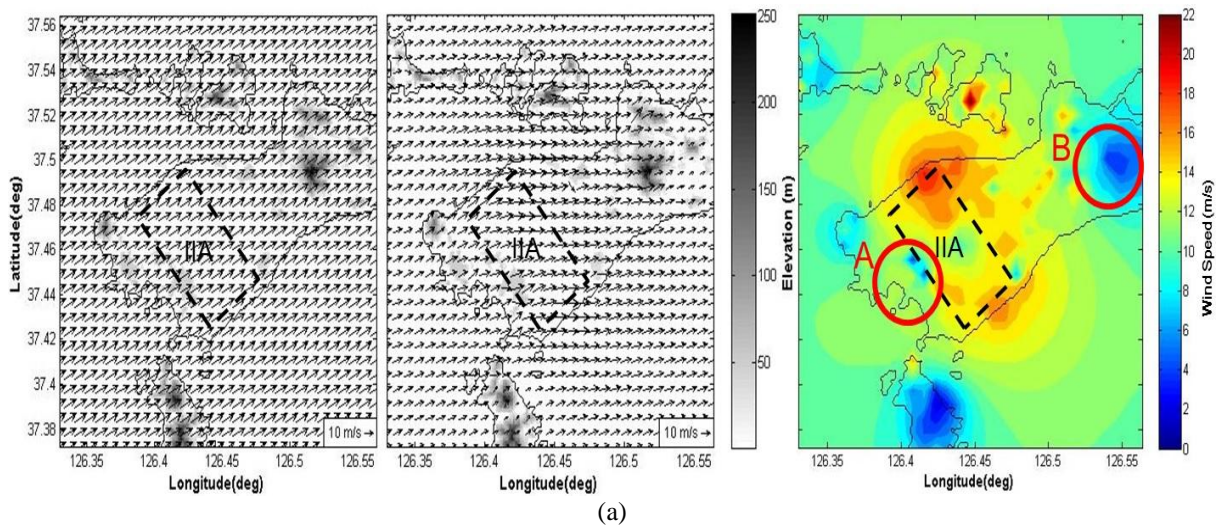
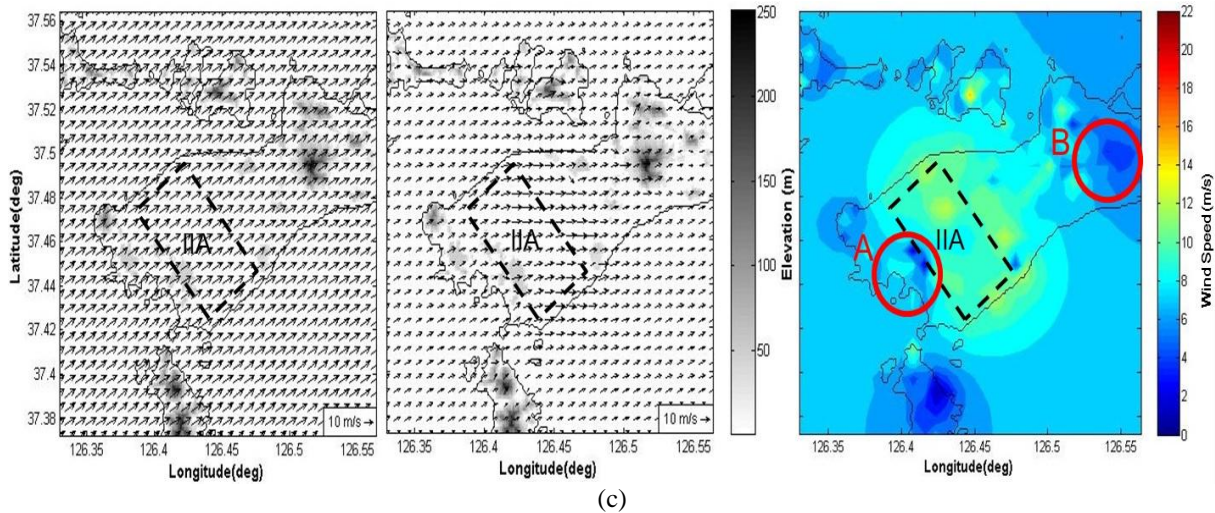


Figure 5. Comparison of wind vector (left) and wind speed (right) fields obtained from the LDAPS (1.5 km resolution) analysis output at 10 m around IIA region on (a) 1200 UTC May 3 and (b) 0000 UTC May 4 2016. The gray color bar indicates topographical height over the model domains. The black contour lines are topography of the LDAPS domain, and dashed rectangular denoted IIA indicate the boundary of the Incheon International Airport (IIA).

We can find more complicated wind distributions from the MCWFM (Fig. 6). The wind simulations obtained by only the downscale process with the LDAPS data are also compared to the adjusted ones computed with both of the model and observation data (two vector fields in Fig. 6). The most distinct difference between the two vector figures is that winds around the airport have shifted from southwesterly winds to westerly winds. This change is also found at the five AWS stations scattered around the airport. The decrease in wind velocity caused by terrain is somewhat plotted in the LDAPS simulations, but the results computed in the MCWFM show significantly more pronounced decrease wind velocity near the hill districts (i. e. red thick circle A and B in Fig. 6). The decrease and change in sections with strong wind speeds over time can also be identified in the MCWFM simulation. The westward winds stronger than 10 m/s are moved into the airport runway and continued to appear for 12 hours, which are consistent with the AWS observations in Fig. 4. This ensures that the wind simulation by considering both set of the model and observation data can present more accurate wind flow than the one of the model data only (Gasset et al., 2012).





(c)
 Figure 6. The same as Fig. 5 except for the MCWFM wind vector simulations entered with (left) only LDAPS input, (middle) LDAPS and observation data, and (right) wind speed distribution computed from the both input data consideration. The white-to-black and blue-to-red color bars present orography and wind speed in the simulation domain. The decrease regions (A and B) of wind velocity are marked as red circles on the both side of the airport.

To test the reproducibility of the calculated wind data at a certain point, the wind field is obtained by excluding observation data at the site number 8 of the LLWAS (shown in Fig. 7), and then both of the measurement and model-calculation is compared for that missing point. All wind sensors of the LLWAS are positioned about 762 m apart around the airport runways so that one can directly compare the model-calculations with 100-m grid intervals to the measurements for each site (e.g. personnel communication with a staff of the Aviation Meteorological Office (AMO) in KMA). Figure 8 presents time series of the wind speed and direction of the wind observations (black dot) and calculations from the LDAPS (black line) and the MCWFM (red line) for all LLWAS stations.

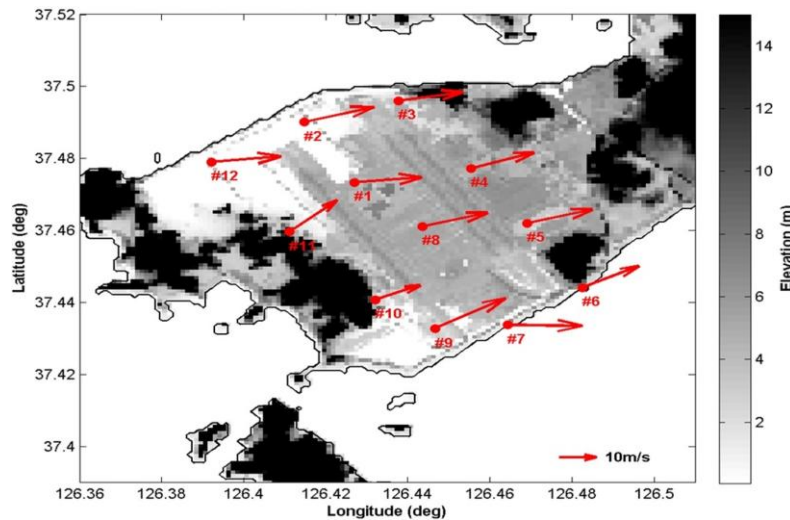


Figure 7. An example of the LLWAS wind distribution at IIA on 1200 UTC May 3, 2016.

The time variation of wind speed reveals that there is a small deterioration in accuracy (e.g. 9.2 m/s which is 1.0 m/s lower than the observation mean of 8.4 m/s) for wind estimations from the LDAPS. However, the mean wind speed from the MCWFM is 7.9 m/s and shows significant increase of the wind speed calculation and its time variation. The model-derived wind direction (bottom plate of Fig. 8) also shows a further increase in skill by estimating the detailed wind speed with both computation and observation data. Especially wind directions computed during the entire period of the event shows that the MCWFM is more consistent with the observed values than the LDAPS. Figure 9 compares the regression values (R2) of wind speed estimated from the observation and each model estimations at the LLWAS site 8 during the strong wind event. As explained above, the R-squared value from the LDAPS accounts for 66.9 % of the wind speed variance while the estimation from the MCWFM accounts for 96.2 %.

This compliance between MCWFM simulation and LLWAS measurement is found in Figure 10. All of the data were computed by entering the wind field the LDAPS output interpolated for the 10-m height and the entire observation material

except that observation site. Overall, the wind speeds are generally consistent with observations, but the values at the points located in front of hills are generally lower. In addition, the wind velocity made at the station of number 10 situated right back of the hill is higher than observation because of addition of the wind crossing over the hill as shown in wind increase region of Figure 6(b). These discrepancies between the model simulation and observations are required more improvements, such as better initialization to account for spatial variability in the input wind field, improvement of turbulence parameterization and databases of the topography and the vegetation (Wang et al, 2005).

4. CONCLUSIONS

The MCWFM is adopted to simulate 100-m resolution wind field over IIA, Korea. It is based on the coupling on the operational LDAPS output and measurements such as AWS and LLWAS at the airport. The downscaled and optimized results are compared against with original input data both of the local-scale model data and the surface observations during the strong wind occurrence from 1700 UTC May 2 to 1000 UTC May 4, 2016. The wind distribution of the 1.5-km LDAPS show some simple reduction of northeastward wind field over the 12 hours. This wind pattern is also found in the 100-m resolution wind simulation from the MCWFM even if there is an estimation process with more detailed topography data. However, the combination of the LDAPS and the observation data, in the context of the high-resolution wind simulation, produces much better results around the airport during the extreme case. In particular, it provides that the wind flow is more likely to the orography effect resulting in decrease of wind speed around the hilly areas of the north and the south of IIA.

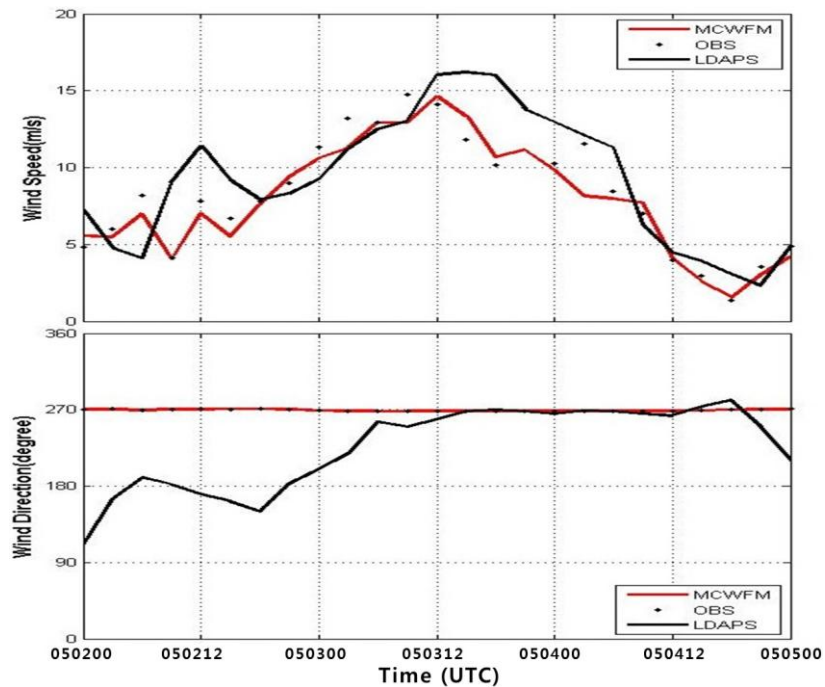


Figure 8. Time series of (top) the wind speed and (bottom) direction obtained from the observation (OBS, block dot) at site number 8 of the LLWAS, and their estimations from the LDAPS (black line) and the MCWFM (red line) at the same measurement altitude of 30 m in IIA during three days (from 0000 UTC May 2 to 0000 UTC May 5, 2016) of the strong wind event.

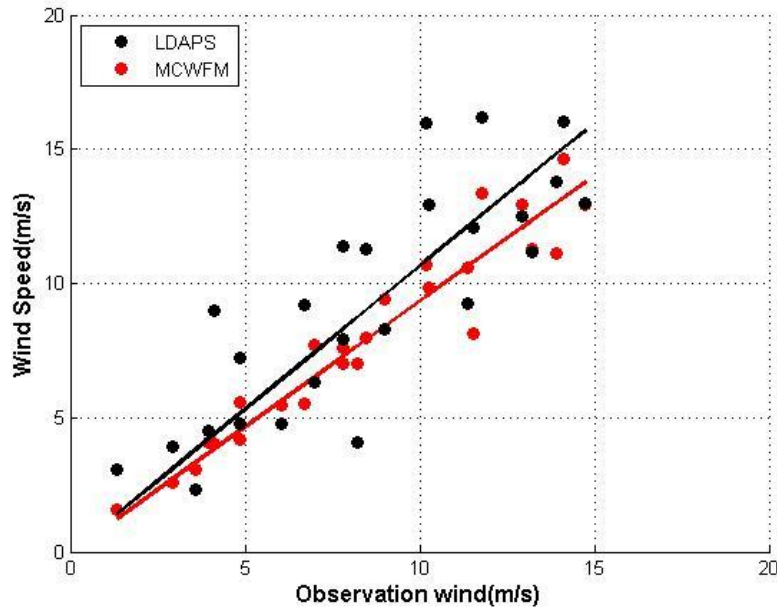
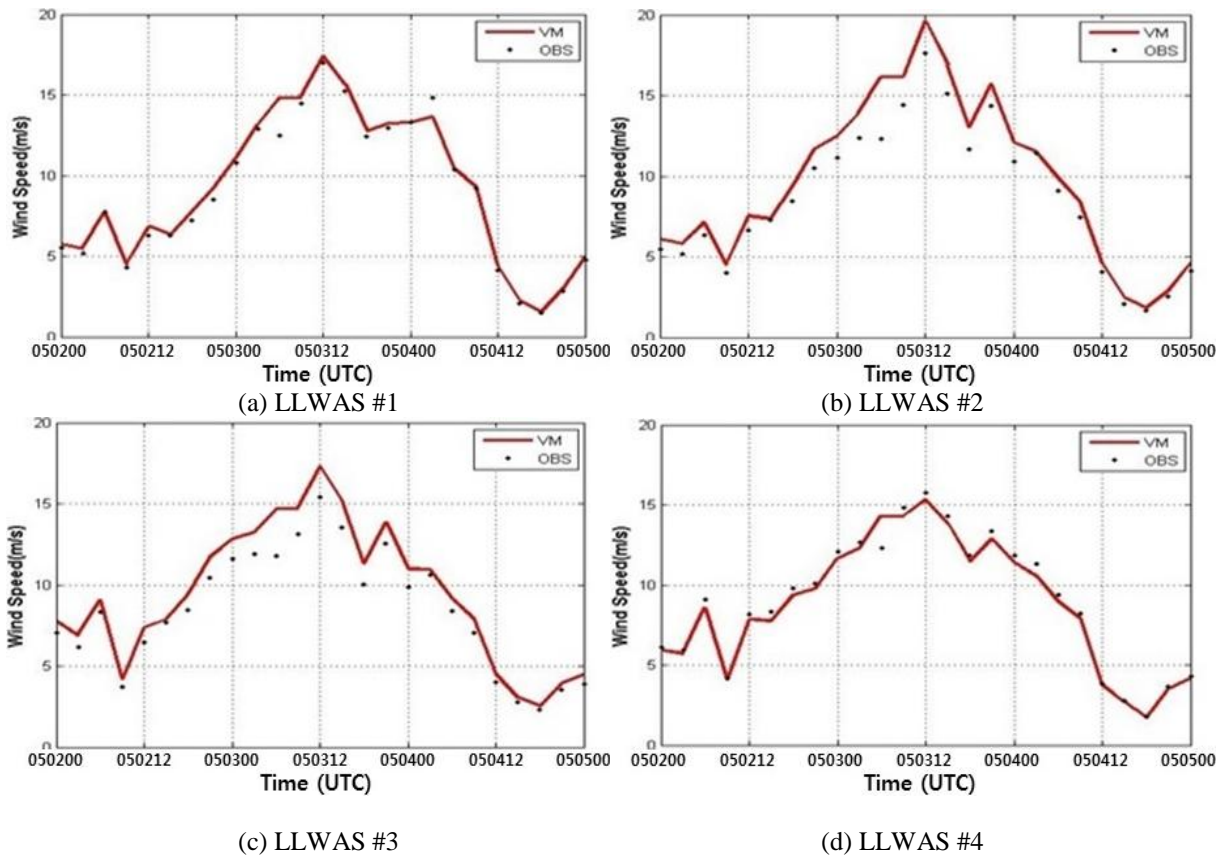


Figure 9. Scattered regression plots (R2) of wind speed for observation vs. model calculations from the LDAPS (black dots and line) and the MCWFM (red dots and line) during the strong wind event shown in Fig. 8.



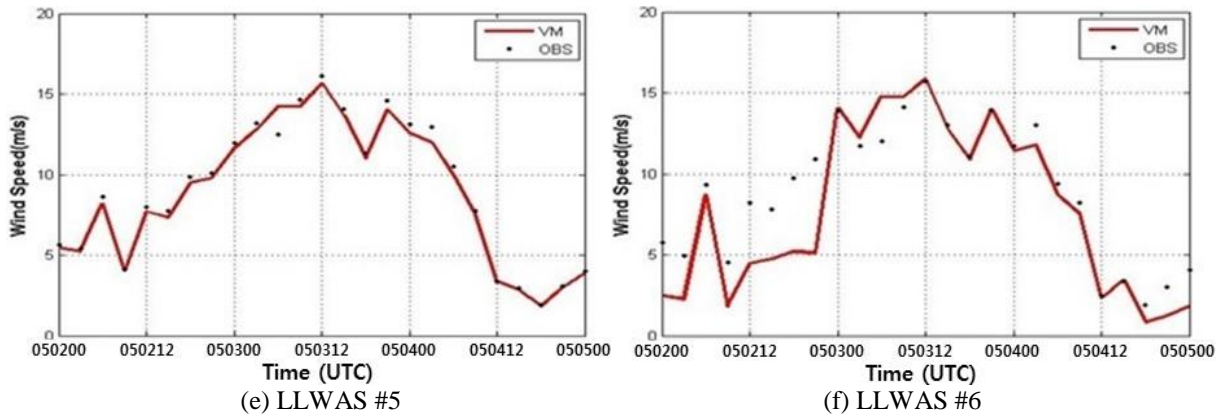
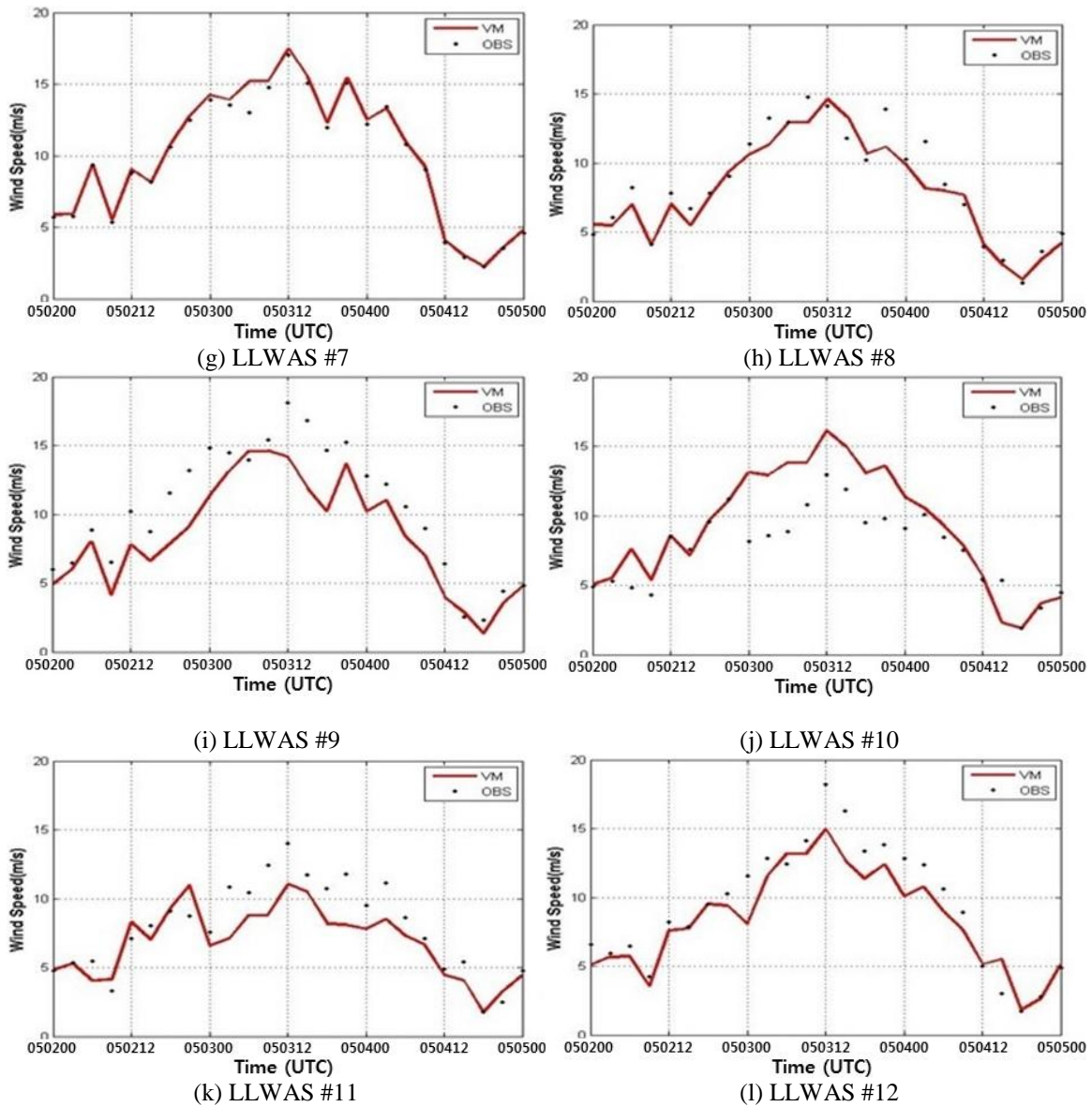


Figure 10. Same time series of wind speed shown in Fig. 8 except for all twelve LLWAS (# 1 ~ # 12) stations and exclusion of the LDAPS comparison on each station. Black dots and solid red lines indicate observation of LLWAS and estimation from the MCWFM.



Continued Figure 10.

The reproducibility experiment of the wind computation is performed by excluding each of twelve observation sites which makes up the LLWAS around the runway of the airport. Mean values of the wind speed at the site number 8, calculated by both models during the wind gust event, are 9.2 m/s and 7.9 m/s respectively, and the latter value is closer to the observation mean of 8.4 m/s. The R-squared value estimated from the comparison between the calculated and measured wind speed values shows MCWFM presents better estimation of 96.2 % to the observations than LDAPS of 66.9 %. The reproducibility of the wind simulation for all twelve LLAWS stations is also checked with comparison of each temporal variations of wind speed, that were simulated by excepting for each specific stations, to that one of measured time series during the gust event. It has to be noted that, in general, the resulting wind velocity is reasonably similar to the measured wind velocity.

Therefore, the overall performance of MCWFM wind simulation seems to be skillful enough to provide more accurate and higher resolution up to 100-m wind fields than the ones from existing operational system. For the situation where the gridded wind simulation data can be viewed in several hours later because of the prediction process, it would be also very useful to meteorologists and dispatchers in airports if these detailed three-dimensional wind data can be taken in less than 8 minutes. However, there are still matters to advance the accuracy of the wind simulation because it is associated with a physical process in the irregular terrain region. These issues will be addressed with more cases of the wind gust in further research and development.

Acknowledgements: This research was funded by the Korea Meteorological Administration Research and Development Program "Research and Development for KMA Weather, Climate, and Earth system Services–Support to Use of Meteorological Information and Value Creation" under Grant (KMA2018-00621).

5. REFERENCES

1. F. Castino, L. Rusca, and G. Solari, "Wind climate micro-zoning: a pilot application to Liguria region (north-western Italy)", *J. Wind. Eng. Ind. Aerodyn.*, 91(11), pp. 1,353-1,357, 2003.
2. P. W. Chan, K. K. Hon, "Performance of super high resolution numerical weather prediction model in forecasting terrain-disrupted airflow at the Hong Kong International Airport: case studies", *Meteor. Appl.*, 23, pp. 101-114, 2016.
3. Federal Aviation Administration (FAA), "Weather-related Aviation Accident Study 2003–2007", Federal Aviation Administration (FAA), 71pp, 2010.
4. M. A. Finney, "FARSITE: Fire Area Simulator-Model Development and Evaluation", USDA Forest Service, Rocky Mountain Research Station, Research Paper RMRS-RP-4, pp. 47, 1998.
5. J. M. Fritsch, "Objective analysis of a two-dimensional data field by the cubic spline technique", *Mon. Wea. Rev.*, 99(5), 379-386, 1971.
6. N. Gasset, M. Lendry, and Y. Gagnon, "A comparison of wind flow models for wind resource assessment in wind energy applications", *Energies*, 5(11), 4, pp. 288-4,322, 2012.
7. W. R. Goodin, G. J. McRae, and J. H. Seinfeld, "A comparison of interpolation methods for sparse data: application to wind and concentration field", *J. Appl. Meteor.*, 18(6), pp. 761-771, 1979.
8. B. Heo, J. Lee, Y. Chu, J. Kim, N. Park, J. Jo, S. Oh, M. Noh and Y. Lee, "Statistical Analysis of AWS Observation Data to Calculate the Quality Control Threshold of Meteorological Observation Data in RQMOD", *Proceedings of Autumn Meeting of KMS*, pp. 390-391, 2005.
9. H. Ishikawa, "Mass-consistent wind model as a meteorological preprocessor for tracer transport models", *J. Appl. Meteor.*, 33(7), pp. 733-743, 1994.
10. L. H. Juárez, M. L. Sandoval, J. López and R. Reséndiz, "Mass Consistent Wind Field Models: Numerical Techniques by L2-Projection Methods, Fluid Dynamics", *Computational Modeling and Applications*, IntechOpen, DOI: 10.5772/2403, pp. 23-40, 2012.
11. P. Kastner-Klein, E. Fedorovich, and M. W. Rotach, "A wind tunnel study of organized and turbulent air motions in urban street canyons", *J. Wind Eng. Ind. Aerodyn.*, 89, pp. 849–861, 2001.
12. T. Kitada, A. Kaki, H. Ueda and L. K. Peters, "Estimation of vertical air motion from limited horizontal wind data – a numerical experiment", *Atmos. Environ.*, 17, pp. 2,181-2,192, 1983.
13. K. Igarashi, and M. Owada, "Numerical analysis of air pollution in a combined field of land/sea breeze and mountain/valley wind", *J. Climate Appl. Meteor.*, 25, pp. 767–784, 1986.
14. Ministry of Land, Infrastructure, and Transport, "Aviation market trend and analysis", Ministry of Land, Infrastructure and Transport, pp. 196, 2016.
15. G. Montero, R. Montenegro, and J.M. Escobar, "A 3-D Diagnostic Model for Wind Field Adjustment", *J. Wind Energy and Industrial Aerodynamics*, 74-76, pp. 249-261, 1998.
16. N. Moussiopoulos and Th. Flassak, "Two vectorized algorithms for the effective calculation of mass-consistent flow fields", *J. Climate Appl. Meteor.*, 25, pp. 847–857, 1986.
17. A. Oliver, E. Rodriguez, J. M. Escobar, G. Montero, M. Hortal, J. Calvo, J. M. Cascon and R. Montenegro, "Wind forecasting based on the HARMONIE model and adaptive finite elements", *Pure Appl. Geophys.*, 172, pp. 109-120, 2015.
18. E. R. Pardyjak and M. J. Brown, "Fast-response modeling of a two building urban street canyon", *Preprints, Fourth Symp. on the Urban Environment*, Norfolk, VA, Amer. Meteor. Soc., CD-ROM, J1.4, 2002.
19. C. F. Ratto, "An overview of mass-consistent models", *Modeling of Atmospheric Flow Field*, World Scientific Publications, pp. 379-400, 1996.
20. R. P. Regmi, "Aviation hazards in the sky over Thada as revealed by meso-scale meteorological modeling", *J. Inst. Sci. Tech.*, 19(2), pp. 65-70, 2014.
21. R. Reiche, M. Robinson, B. Niu, D. O'Donnell, and M. Kay, "Assessment of wind shear forecast performance and implications on wind compression impacts", 17th Conference on Aviation, Range, and Aerospace Meteorology, Phoenix, AZ, pp. 1-7, 2015.
22. C. A. Sherman, "A mass-consistent model for wind fields over complex terrain", *J. Appl. Meteor.*, 17(3), pp. 312-319, 1978.
23. R. M. Traci, G. T. Phillips and P. C. Patnaik, "Developing a site selection methodology for wind energy conversion systems", DOE/ET/20280-3, [N.T.I.S., Springfield, Virginia], pp. 296, 1978.
24. C. W. Wang, D. Garvey, S. Chang, and J. Cogan, "Application of a multigrid method to a mass-consistent diagnostic wind model", *J. Appl. Meteor.*, 44(4), pp. 1,078-1,089, 2005.